applied sciences

MDPI

Article

An Improved High-Resistance Fault Detection Method in DC Microgrid Based on Orthogonal Wavelet Decomposition

Liuming Jing *, Tong Zhao, Lei Xia and Jinghua Zhou

Power Electronics & Motor Drivers Engineering Research Center of Beijing, North China University of Technology, Beijing 100144, China

* Correspondence: lmjing@ncut.edu.cn

Abstract: High-resistance faults in direct current (DC) microgrids are small and thus difficult to detect. Such faults may be "invisible" in that grid operation continues for a considerable time, which damages the grid. It is essential to detect and remove high-resistance faults; we present a detection method herein. First, the transient DC current during the fault is subjected to hierarchical wavelet decomposition to identify high-resistance faults accurately and sensitively; the wavelet coefficients are detected using the singular value decomposition (SVD) method. The SVD valve can denoise the dc microgrid fault current, which eliminates the influence of converter switching frequency and background noise effectively. Power system computer-aided design (PSCAD)/electromagnetic transients including direct current (EMTDC)-based simulations showed that our method successfully identified high-resistance faults.

Keywords: DC microgrid; high-resistance fault; orthogonal wavelet transformation; Cassie model; PSCAD/EMTDC

Citation: Jing, L.; Zhao, T.; Xia, L.; Zhou, J. An Improved High-Resistance Fault Detection Method in DC Microgrid Based on Orthogonal Wavelet Decomposition. *Appl. Sci.* **2023**, *13*, 393. https://doi.org/10.3390/app13010393

Academic Editors: Luigi Fortuna and Andreas Sumper

Received: 5 December 2022
Revised: 26 December 2022
Accepted: 26 December 2022
Published: 28 December 2022

1. Introduction

Direct current (DC) microgrids exhibit many advantages compared to AC (alternating current) grids; the voltage is lower, less electric power is lost, supply reliability is high, and distributed generation is simple. It is more suitable to choose DC microgrids for interconnecting renewable resources.

However, DC microgrids have some challenges attached to them, such as that of the fault protection. The DC current increases rapidly after a fault, which is challenging for existing protective systems that fail to locate and isolate faults. DC microgrids contain a variety of electronic devices generally concentrated within small areas, such as ships, islands, grasslands, and data centers; the environmental conditions in these areas may be challenging [1,2].

Therefore, DC microgrid cable faults occur frequently because of insulation degradation and breakdown. Line insulator damage, overheating of energy storage elements, loose joints, aging wires, and environmental stress can cause two types of faults: pole-to-pole faults (short circuits) and pole-to-ground faults [3].

The impedance caused by pole-to-pole faults is small because the conductors are directly connected at the fault point. In contrast, pole-to-ground faults often show high resistance (HR) because the conductor connects with the ground via the insulation [4]. During such faults, converter operation may continue, triggering a fault cascade involving cables or converters. Therefore, whenever an HR fault (HRF) occurs, an operator must be informed and then act [5,6]. After a metal or small-resistance fault, the fault current increases quickly to a prominent peak that is easy to detect; the fault can then be rapidly removed. However, after an HRF, the electrical parameters do not obviously change, making it difficult to detect the fault [7–9].

Due to the small damping of the DC microgrid line, the fault may spread and affect adjacent circuits, such as photovoltaic modules, energy storage systems, lines, control

systems, etc., which will be damaged; this results in the fault operation of the DC microgrid, which will pose a serious threat to personal safety and equipment safety and may even cause accidents such as fires [10,11]. Therefore, accurate detection and effective treatment of high resistance faults are important conditions to ensure the safe and stable operation of DC microgrids [12].

Existing HRF detection methods [13] use mathematical morphology (MM; two elementary transformations) to detect faults in low-voltage DC (LVDC) distribution systems. However, arc faults are not well-detected. An in-depth analysis [14] yielded the optimal parameters for the detection of serious arc faults. The energies with and without arc faults were compared to determine the effects of combinations of three parameters on arc fault detection. However, this is not practical in the field. A transient algorithm [15] has been used for HRF detection; a discrete wavelet transform is employed to monitor the high- and low-frequency voltage components at several points. The utility of the method was verified by simulation. However, it cannot be applied to a DC grid.

An impedance measurement algorithm for equivalent load detection in DC microgrids has been developed [16]: the power converter injects small signal oscillations into the DC bus throughout the duty cycle and an LIA (lock in amplifier) isolates the oscillations and measures the equivalent incremental impedances. However, dedicated hardware is required and it is difficult to distinguish overloads from faults. HRF can be detected using a data-mining decision tree [17] and implemented in a distribution network. But the interference problem of communication needs to be considered. A protection method based on the time and polarity of initial current traveling waves is proposed for transmission lines in [18]. However, the calculation process is complicated and requires a high communication speed. The proposed algorithm calculates the fault distance based on the characteristics of the voltage resonance in [19]. It presents an intelligent scheme for high impedance fault detection using mathematical morphology and decision tree in [20]. However, the methods of [19,20] are computationally complex and their reliability remains to be verified. There are also arc characteristic identification method [21], circuit analysis method [22,23], artificial intelligence method [24], etc.

In summary, HRFs are difficult to detect and may cause serious harm; few practical detection methods are available. In this paper, a fault detection method by combining singular value decomposition (SVD) with orthogonal wavelet fusion in the time–frequency domain was proposed and used to analyze the characteristics of HRFs in a DC microgrid. This paper presents the detection method, evaluates its utility, and provides our conclusions.

The main innovations of this paper are as follows:

(1) This paper establishes a DC arc simulation model for high resistance faults in DC microgrids.
(2) A detection method decomposes high frequency waveforms using orthogonal wavelets. The fault characteristics of the fault time domain are analyzed.
(3) The amplitude of the wavelet coefficients is detected using the SVD. The Hankel-SVD can eliminate the specified switching frequency and the background noise, it can avoid the influence of the inverter noise and other electrical noise on the extraction of HRF characteristics.

The rest of this paper is organized as follows: the second part is the HRF modeling of the DC microgrid; the third part analyzes high resistance fault characteristics; the fourth part is the HRF detection; the fifth part is the experimental verification; and the sixth part is the conclusion.

2. HRF Modeling of DC Microgrid

DC microgrid HRFs are usually arc high resistance faults. DC arcs can be series or parallel arcs, the latter of which develop when the two potentials change after damage to the insulation. The arc resistance grounding is parallel and is affected by the arc voltage, arc current, discharge gap, and arc length, among other factors. The main arc models are the Cassie and Mayr models; the latter simulates arc ignition and extinguishment. The

Cassie model can handle the continuous arc burning of a DC. Arc resistance is affected by the energy relationship between the arc voltage and arc current.

In Equation (1), $Q(\mathrm{MW{\cdot}S} = \mathrm{MJ})$ is the energy stored in the arc, $P(\mathrm{MW})$ is the dissipation power, and $u(\mathrm{kV})$ and $i(\mathrm{kA})$ are the arc voltage and current, respectively. Equation (1) shows that arc energy is gradually dissipated during combustion.

$$\frac{\mathrm{d}Q}{\mathrm{d}t} = u{\cdot}i - P \tag{1}$$

Equation (1) can be transformed to quantify the relationship between the rate of change of arc unit conductivity g and that of arc power:

$$\frac{\mathrm{d}Q}{\mathrm{d}g}{\cdot}\frac{\mathrm{d}g}{\mathrm{d}t} = \frac{1}{P^{-1}}(\frac{g{\cdot}u^2}{P} - 1) \tag{2}$$

$$\frac{1}{g}{\cdot}\frac{\mathrm{d}g}{\mathrm{d}t} = \frac{1}{g{\cdot}P^{-1}{\cdot}(\frac{\mathrm{d}Q}{\mathrm{d}g})}(\frac{g{\cdot}u^2}{P} - 1) \tag{3}$$

Let $\tau = g{\cdot}P^{-1}{\cdot}\frac{\mathrm{d}Q}{\mathrm{d}g}$; Equation (3) can now be simplified to yield Equation (4):

$$\frac{\mathrm{d}\ln g}{\mathrm{d}t} = \frac{1}{\tau}(\frac{g{\cdot}u^2}{P} - 1) \tag{4}$$

Let E be the arc voltage gradient, P_0 the power emitted by the arc per unit volume, and σ the arc conductivity. These parameters are related Equation (5):

$$E^2 = \frac{P_0}{\sigma} \tag{5}$$

Substituting Equation (5) into Equation (4) yields Equation (6):

$$\frac{\mathrm{d}\ln g}{\mathrm{d}t} = \frac{1}{\tau_c}(\frac{u^2}{E^2} - 1) \tag{6}$$

where τ_c is the time constant of the Cassie model. Equation (7) shows the Cassie model arc resistance:

$$R_{arc} = \mathrm{e}^{\frac{1}{\tau_c}\int(1-\frac{u^2}{E^2})\mathrm{d}t} \tag{7}$$

During an HRF, an arc occurs after the breakdown of the air gap between the line and ground; the arc resistance is in series with that of the ground. In the Cassie model, arc combustion stabilizes when the voltage between the arc and ground reaches a certain value. As the arc and grounding point resistance are connected in series, the grounding medium consumes some energy, rendering the arc current small and thus increasing the overall arc resistance.

3. Analysis of High Resistance Fault

The voltage source converter is an important component of a DC microgrid. If a DC line fault occurs, it is propagated through the capacitor discharge, diode free conduction and power grid side-feed flow stages. Most HRFs are single-pole grounding faults; thus, one should focus on these faults. A schematic of the capacitor discharge stage is shown in Figure 1.

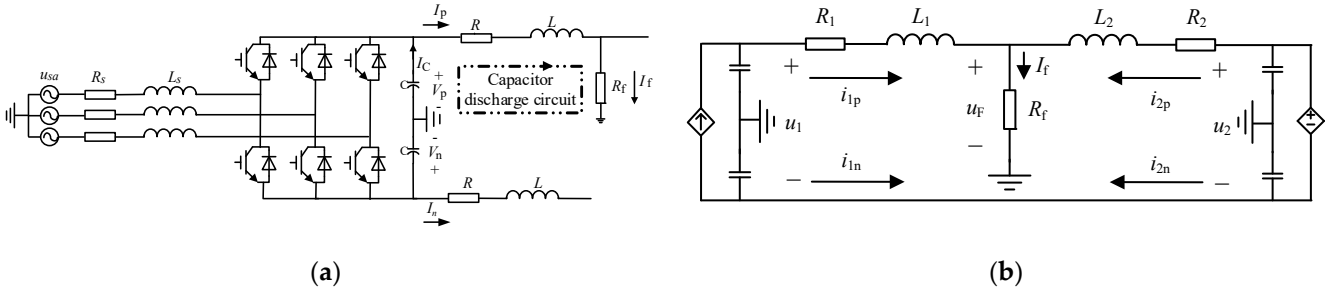

Figure 1. Schematic diagram of the capacitor discharge stage during high resistance fault. (**a**) capacitor discharge stage circuit; (**b**) equivalent diagram.

As in the capacitor discharge phase, capacitor C discharges after a fault occurs; the initial voltage V_p is equal to the normal line-end voltage; I_c is the capacitor discharge current; R and L are the equivalent resistance and line equivalent inductance from the capacitor to the fault point, respectively; R_f is the fault resistance; and I_f is the current flow. The fault resistance current at this stage is the capacitive discharge current. The time-domain expression of the discharge current is given by:

$$i(t) = \frac{V_c(0)}{L(s_2 - s_1)}[e^{-s_1 t} - e^{-s_2 t}] + \frac{i_L(0)}{s_2 - s_1}[-s_1 e^{-s_1 t} + s_2 e^{-s_2 t}] \tag{8}$$

s_1, s_2 is given by:

$$s_{1,2} = -\alpha \pm \sqrt{\alpha^2 - \omega_0^2} \tag{9}$$

The damping coefficient α and resonance frequency ω_0 are given by Equations (10) and (11), respectively:

$$\alpha = \frac{R + R_f}{2L} \tag{10}$$

$$\omega_0 = \frac{1}{\sqrt{LC}} \tag{11}$$

Substituting arc resistance into the Equation (10), yields Equation (12):

$$\alpha = \frac{R + e^{\frac{1}{\tau_c}\int (1 - \frac{u_F^2}{E^2})dt}}{2L} \tag{12}$$

After HRFs, the fault response curves are overdamped, the transient response times are short, and the peak responses are small, unlike after metallic and low-resistance faults. During the grid-side current-feeding stage, the AC side transmits current via the voltage source converter bridge arm to the DC fault; the equivalent circuit is shown in Figure 2.

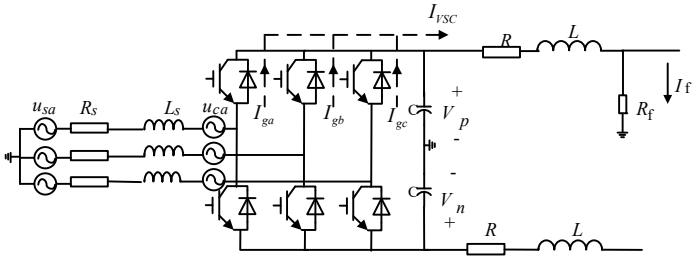

Figure 2. Schematic diagram of the power grid side feeding stage.

If an HRF persists, the converter will lock up, then becoming equivalent to an uncontrolled rectifier bridge. The current at the fault point is the sum of the diode bridge arm currents, which can be written as:

$$i_{VSC} = i_{D1} + i_{D2} + i_{D3} = i_{\mathrm{ga}} + i_{\mathrm{gb}} + i_{\mathrm{gc}} \tag{13}$$

where i_{ga}, i_{gb}, and i_{gc} are the three-phase currents of AC, respectively, i.e., the current passing through the diode bridge arm when a positive value is selected. Taking phase A as an example, Equations (14)–(17) are applied:

$$i_{\mathrm{ga}} = I_{\mathrm{g}} \sin(\omega_s t + \alpha - \varphi) + I_{\mathrm{gn}} e^{\frac{-t}{\tau}} \tag{14}$$

$$\varphi = \arctan\left[\frac{\omega_s (L_{\mathrm{ac}} + L)}{R + R_{\mathrm{f}}}\right] \tag{15}$$

$$\tau = \frac{L_{\mathrm{ac}} + L}{R + R_{\mathrm{f}}} \tag{16}$$

$$I_{\mathrm{gn}} = \left[I_{\mathrm{g}|0|} \sin(\alpha - \varphi_0) - I_{\mathrm{g}} \sin(\alpha - \varphi)\right] \tag{17}$$

where $I_{\mathrm{g}|0|}$ is the amplitude of the initial grid current; φ_0 is the impedance angle; L_{ac} is the AC-side inductance; α is the AC phase angle; and I_{g} is the amplitude of the periodic component of the short-circuit current. After an HRF, the zero-mode current is extracted, and the transient zero mode current is calculated as follows:

$$i_0 = \frac{\sqrt{2}}{2}(i_{1\mathrm{p}} + i_{1\mathrm{n}}) \tag{18}$$

The frequency domain component of the current in the Cassie DC arc model decreases with increasing frequency. After the arc current is superimposed, the amplitude of the corresponding frequency band changes. Thus, phase decomposition of the low frequency band reveals the amplitude change, allowing arc resistance fault detection with a low arc current.

4. HRF Detection

Based on the above, time–frequency domain detection method was used to extract the characteristics of arc HRFs. Orthogonal wavelet transformation and singular value decomposition (SVD) extract information in the time and frequency domains, respectively. After orthogonal wavelet transformation, the original signal is decomposed into various components at different scales when h is a wavelet-based low-pass filter, g is a wavelet based high-pass filter, $a_j(n)$ is the low-frequency part of the signal, and $d_j(n)$ is the high-frequency part of the signal. As the decomposition time increases, $a_j(n)$ and $d_j(n)$ are given by Equations (19) and (20), respectively:

$$a_{j+1}(n) = \sum_k h(k - 2n) a_j(k) \tag{19}$$

$$d_{j+1}(n) = \sum_k g(k - 2n) a_j(k) \tag{20}$$

where k is the length of the filter, n is the length of the signal, and j is the number of decompositions. The upper-stage signal is successively processed by the low- and high-pass filters, yielding the lower stage low- and high-frequency signals. The decomposition is shown in Figure 3.

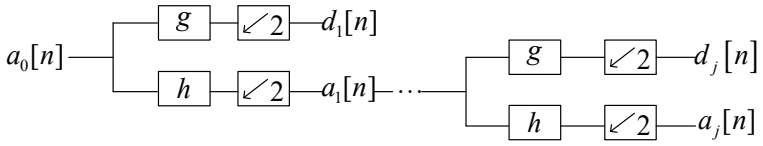

Figure 3. Orthogonal wavelet decomposition.

After wavelet transformation, SVD is used to distinguish signals of different frequency bands; this can be applied to decompose non-square matrices, and it is assumed that matrix A is an m*n-order matrix. There then exists an m*n-order orthogonal matrix U and m*n-order orthogonal matrix V, so that Equation (21) holds:

$$A = UDV^T \tag{21}$$

where D is an $m \times n$-order diagonal matrix and $D = (diag(\sigma_1, \sigma_2, \ldots, \sigma_q), O)$. The diagonal element $\sigma_1, \sigma_2, \ldots, \sigma_q$ is the singular value of matrix A. Common forms of matrix A include the Toeplitz, cycle, and Hankel matrices; the latter was used. During SVD, the phase of the decomposed semaphore in the original signal remains unchanged; in other words, the decomposition simply subtracts the decomposed signal from the original signal. The Hankel matrix of the original signal $y(n)$ is given by Equation (22):

$$A = \begin{bmatrix} y(1) & y(2) & \cdots & y(n) \\ y(2) & y(3) & \cdots & y(n+1) \\ \vdots & \vdots & \vdots & \vdots \\ y(m) & y(m+1) & \cdots & y(N) \end{bmatrix} \tag{22}$$

where $u_1, u_2, \ldots, u_q$ are the elements in matrix u of order m*1, and $v_1, v_2, \ldots, v_q$ are the elements in matrix v of order n*1. Orthogonal wavelet transformation is combined with SVD for time-frequency domain decomposition. First, the current signal (collected on the line) is decomposed at various scales to obtain coefficients that are used to construct a Hankel matrix; SVD then yields singular value spectra at different wavelet decomposition scales. Among the frequency domain ranges represented by each scale after wavelet decomposition, $a_j[n]$ decomposed to layer j is the lowest-frequency region.

If the DC arc current is small, most current energy is of low frequency. After an HRF fault, an obvious gain change will be seen at low frequency. The amplitude of random line noise is usually small and can thus be ignored. The arc frequency band is predominantly low-frequency, and the line high-frequency components do not interact.

Then sum the singular value amplitudes of all points of the low-frequency singular value sequence of the jth layer decomposed by the wavelet; thus, sum the singular value of the $a_j[n]$ layer of the fault line and singular value sequence of the $a_j[n]$ layer of the non-fault line at least k times. The fault detection criterion is represented by Equation (23):

$$a_{j\_\text{fault}}\left[\sum_{i=1}^{q}\sigma_i\right] > a_{j\_\text{Non fault}}\left[\sum_{i=1}^{q}\sigma_i\right] \tag{23}$$

A flow chart of the time-frequency domain detection method is shown in Figure 4.

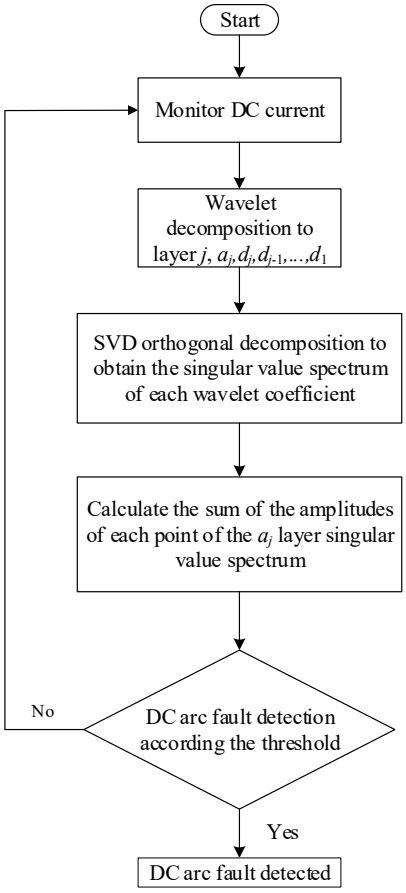

Figure 4. Flow chart of arc resistance detection.

5. Experimental Verification

The simulation model of the DC microgrid built using PSCAD/EMTDC is shown in Figure 5. At the sending ends, the transmission terminal is in constant power (PQ) control mode and the receiving terminal is in constant DC voltage (U_{dc}) control mode. The DC microgrid voltage is 1.2 kV and the transmission power is 0.5 MW [25,26].

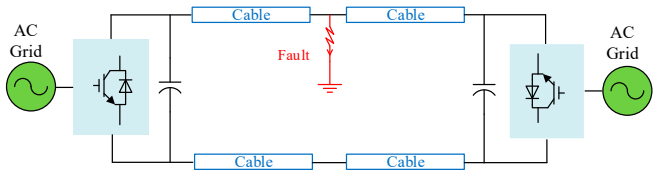

Figure 5. A two-port DC microgrid.

The parameters and cable lengths of each element are shown in Table 1. A DC cable and bipolar connections were used.

Table 1. DC microgrid model parameters.

Parameter	Value
DC line voltage	1.25 kV
Cable resistance	0.02 ohm/km
Cable inductance	7.68×10^{-6} H/km

The DC arc current is nonlinear; changes in amplitude are not obvious at HRF. The amplitude frequency variations of various arc currents are shown in Figure 6. As the arc current increases, so too does the high-frequency component; the current amplitude

decreases when the frequency increases. The frequency-domain characteristics of arc current were directly related to the amplitude. When the amplitude is low, the frequency fluctuates. Therefore, the Cassie model can represent a DC arc under a low arc current.

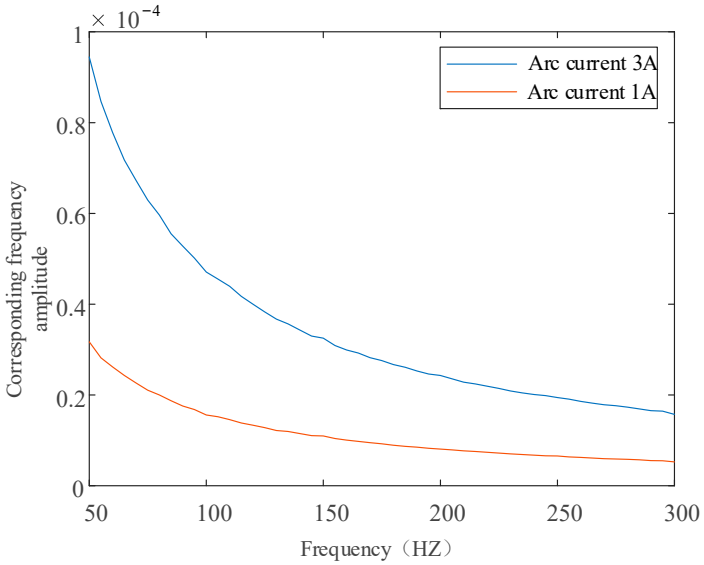

Figure 6. The DC arc current spectrum.

The arc resistance current depends on the arc voltage. During simulation, the arc current was affected mainly by the grounding point in series with the arc resistance. The fault time was 3 s, the arc resistance ground connection was 100 ohm, the fault distance was 1 km, and the interaction voltages were 160 and 200 V. The amplitude and frequency characteristics of the normal and line currents grounded by the arc resistance are shown in Figure 7.

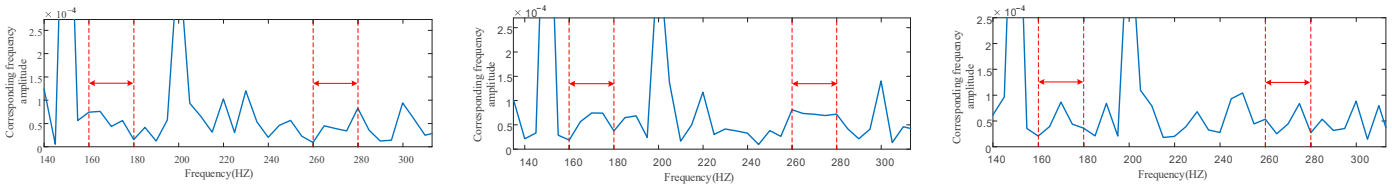

(**a**) (**b**) (**c**)

Figure 7. Amplitude frequencies of the normal and arc-resistance grounding fault currents: (**a**) Normal current amplitudes and frequency characteristics; (**b**) amplitude frequency characteristics when the inter-arc voltage was 160 V and the grounding resistance was 100 ohm; (**c**) amplitude frequency characteristics when the inter-arc voltage was 200 V and the grounding resistance 100 ohm.

Comparison of Figure 8a,b shows that, after grounding, the frequency amplitudes at lower layer increased, as did the arc voltages. The amplitudes of the line current changes were in line with this analysis. Time-based frequency-domain analyses are commonly used to explore arc resistance grounding, with wavelet decomposition then applied to extract the characteristics thereof. Analysis of the detail wavelet coefficients is preferred via decomposition to five layers, of which d5 is the special frequency layer (in which arc current amplitudes typically increase). This layer yields valuable information about arc frequency decomposition. The decomposed fault current is shown in Figure 8.

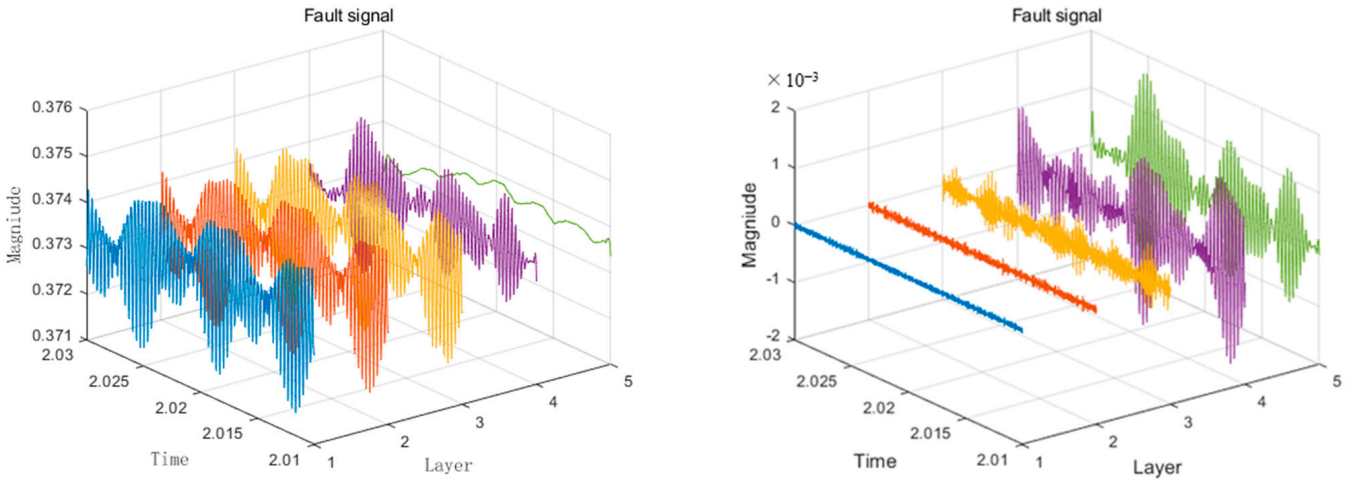

(**a**) (**b**)

Figure 8. Wavelet decomposition diagram of the fault current: (**a**) approximation coefficients; (**b**) detail coefficients.

Wavelet decomposition does not directly yield frequency data. Thus, after collecting the decomposition data of all components of the frequency domain, The Hankel matrix was constructed and subjected to SVD, which yielded normal and arc currents with 30 single values (Figure 9).

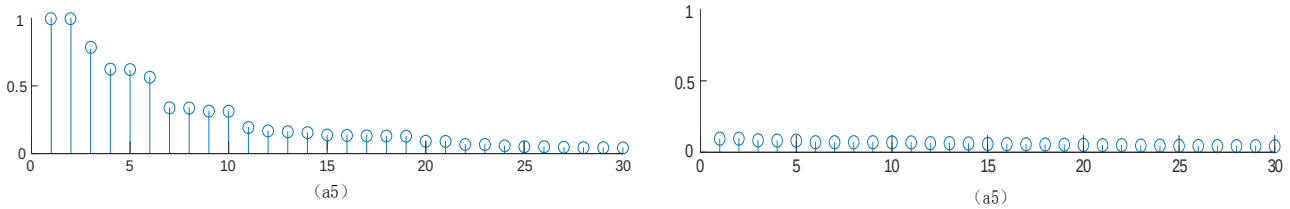

(**a**) (**b**)

Figure 9. SVD of the (**a**) arc and (**b**) normal currents.

The singular value arrangement was guided mainly by the wavelet decomposition scale scores, using a5 as the feature contrast sequence. The effect of the arc current was then apparent; the top 10 a5 singular points on the fault current SVD decomposition graph exhibited obvious amplitude changes, reflecting the amplitude of the DC low-frequency band and low arc current amplitude. Figure 10 shows the result of fault signal after denoising the specified converter switching frequency and the background noise.

Table 2 shows the time-domain data for different fault situations. The detection threshold was selected based on the normal current value, i.e., 27. The test results exceeded this threshold; thus, our time-domain detection method effectively detects arc resistance faults.

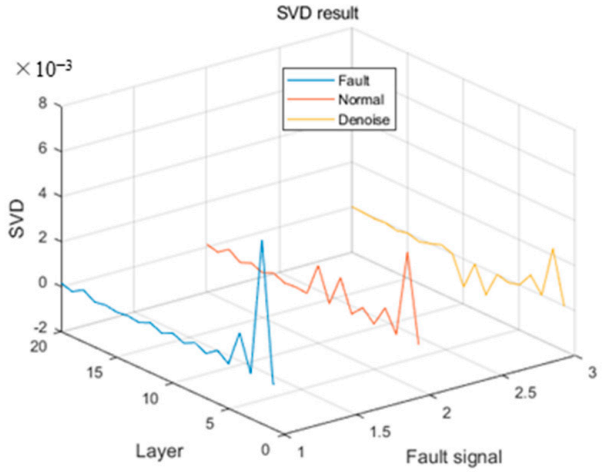

Figure 10. SVD valve after denoising.

Table 2. Results of our time-domain detection method obtained under different fault conditions.

Fault Distance	Resistance: 100 ohm Arc Voltage: 200 V	Resistance: 100 ohm Arc Voltage: 250 V	Resistance: 300 ohm Arc Voltage: 200 V
1 km	277.5936	277.3821	275.9747
3 km	277.9686	278.8989	277.1487
5 km	276.1013	275.4974	275.1601
7 km	276.1919	276.6416	275.4519

In order to verify the ability of the time–frequency detection method to detect arc resistance, its reliability is tested by setting the fault resistance, fault distance, and inter arc voltage with different resistance values. The average value and standard deviation of singular value under different fault conditions are shown in Tables 3 and 4.

Table 3. Mean value of low frequency singular value under different fault conditions.

Fault Distance	Resistance: 100 ohm Arc Voltage: 200 V	Resistance: 100 ohm Arc Voltage: 250 V	Resistance: 300 ohm Arc Voltage: 200 V
1 km	0.0427	0.044	0.0422
3 km	0.0427	0.0446	0.0432
5 km	0.046	0.0427	0.0417
7 km	0.0427	0.0416	0.0428

Table 4. Standard deviation of singular value in low frequency layer under different fault conditions.

Fault Distance	Resistance: 100 ohm Arc Voltage: 200 V	Resistance: 100 ohm Arc Voltage: 250 V	Resistance: 300 ohm Arc Voltage: 200 V
1 km	0.0483	0.0494	0.0477
3 km	0.0411	0.0446	0.0474
5 km	0.0501	0.0477	0.0480
7 km	0.0423	0.0472	0.0443

To verify the ability of time-frequency detection method. We compared the wavelet method with other methods such as the S-transform-based method, the Short Time Fourier transform-based method, and the Wigner–Ville distribution-based method. As shown in the Figure 11, the proposed wavelet-based method can better extract the fault characteristics.

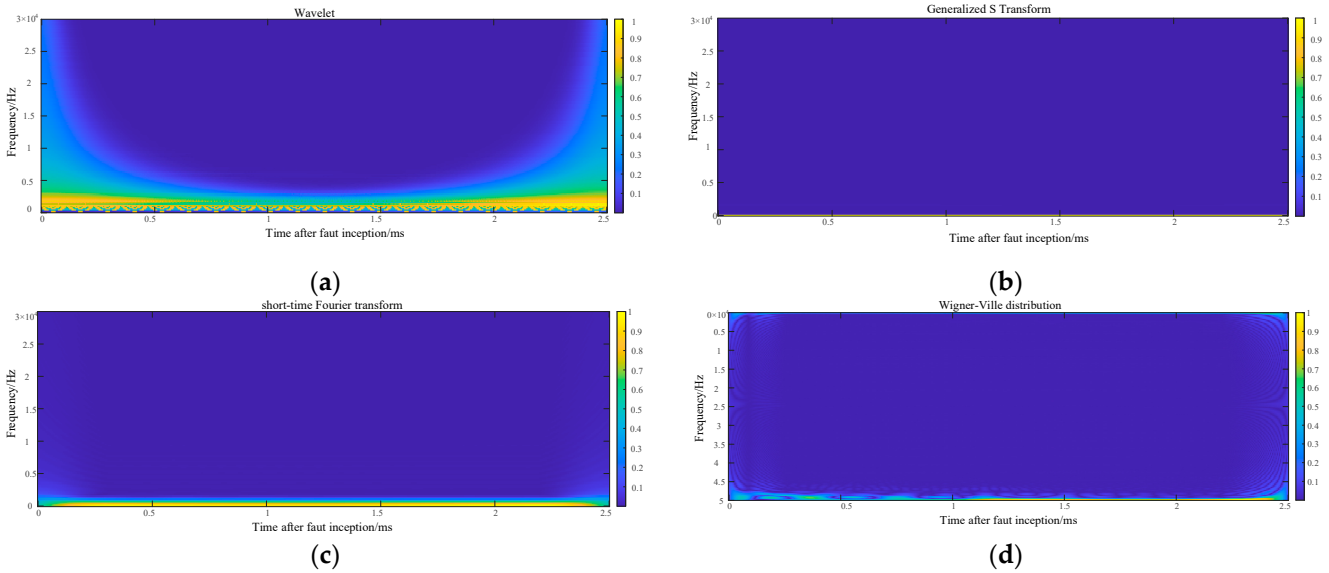

Figure 11. Simulation results comparison: (**a**) Wavelet based method (**b**) S-transform based method (**c**) Short Time Fourier transform based method (**d**) Wigner-Ville distribution-based method.

6. Conclusions

In this paper, an HRF fault detection method for DC microgrids was proposed. This method uses wavelet decomposition to improve the speed and sensitivity of fault detection. The fault characteristics of HRF are weak. This method uses the singular value decomposition to extract information in the time and frequency domains. The Hankel-SVD can eliminate the specified converter switching frequency and the background noise, and it can avoid the influence of the inverter noise and other electrical noise on the extraction of HRF characteristics. The DC microgrid and high-resistance arc fault models were created using PSCAD/EMTDC, and the proposed detection method was verified by changing the high resistance fault occurrence position and the resistance value. The simulations showed that the proposed method can correctly judge the HRF fault information.

Author Contributions: L.J. supervised the study and coordinated the main theme of this paper. T.Z. prepared the manuscript and completed the simulations. L.X. developed the model of DC microgrid in the study. J.Z. discussed the results and implications, and commented on the manuscript. All authors have read and agreed to the published version of the manuscript.

Funding: This research was funded by Beijing Natural Science Foundation, grant number 3214060.

Institutional Review Board Statement: Not applicable.

Informed Consent Statement: Informed consent was obtained from all subjects involved in the study.

Data Availability Statement: The data used to support the findings of this study are available from the corresponding author upon request.

Conflicts of Interest: The authors declare no conflict of interest.

References

1. Jalil, M.; Samet, H.; Ghanbari, T.; Tajdinian, M. An Enhanced Cassie–Mayr-Based Approach for DC Series Arc Modeling in PV Systems. *IEEE Trans. Instrum. Meas.* **2021**, *70*, 1–10. [CrossRef]
2. Christen, T.; Ranjan, N. Generalized Mayr Model for Arcs in MV Switches with Splitter Plates. *IEEE Trans. Power Deliv.* **2022**, *37*, 359–364. [CrossRef]
3. Gao, H.; Wang, Z.; Tang, A.; Han, C.; Guo, F.; Li, B. Research on series arc fault detection and phase selection feature extraction method. *IEEE Trans. Instrum. Meas.* **2021**, *70*, 1–8. [CrossRef]
4. Jiang, R.; Bao, G.; Hong, Q.; Booth, C.D. A coupling method for identifying arc faults based on short-observation-window SVDR. *IEEE Trans. Instrum. Meas.* **2021**, *70*, 1–10. [CrossRef]

5. Amiri, A.; Samet, H.; Ghanbari, T. Recurrence plots based method for detecting series arc faults in photovoltaic systems. *IEEE Trans. Ind. Electron.* **2021**, *69*, 6308–6315. [CrossRef]
6. Xiong, Q.; Feng, X.; Gattozzi, A.L.; Liu, X.; Zheng, L.; Zhu, L.; Ji, S.; Hebner, R.E. Series arc fault detection and localization in DC distribution system. *IEEE Trans. Instrum. Meas.* **2020**, *69*, 122–134. [CrossRef]
7. Alam, M.K.; Khan, F.; Johnson, J.; Flicker, J. A comprehensive review of catastrophic faults in PV arrays: Types detection and mitigation techniques. *IEEE J. Photovolt.* **2015**, *5*, 982–997. [CrossRef]
8. Lu, S.; Phung, B.T.; Zhang, D. A comprehensive review on DC arc faults and their diagnosis methods in photovoltaic systems. *Renew. Sustain. Energy Rev.* **2018**, *89*, 88–98. [CrossRef]
9. Gammon, T.; Lee, W.-J.; Zhang, Z.; Johnson, B.C. A review of commonly used DC arc models. *IEEE Trans. Ind. Appl.* **2015**, *51*, 1398–1407. [CrossRef]
10. Kim, Y.-J.; Kim, H. Modeling for series arc of DC circuit breaker. *IEEE Trans. Ind. Appl.* **2019**, *55*, 1202–1207. [CrossRef]
11. Gaunce, A.C.; Wu, X.; Mandeville, J.D.; Hoffman, D.J.; Khalsa, A.S.; Sottile, J.; Wellman, R.J. DC arc flash: Testing and modeling incidents in a 125-V substation battery backup system. *IEEE Trans. Ind. Appl.* **2020**, *56*, 2138–2147. [CrossRef]
12. Ahmadi, M.; Samet, H.; Ghanbari, T. Kalman filter-based approach for detection of series arc fault in photovoltaic systems. *Int. Trans. Electr. Energy Syst.* **2019**, *29*, e2823. [CrossRef]
13. Oh, Y.-S.; Han, J.; Gwon, G.-H.; Kim, D.-U.; Noh, C.-H.; Kim, C.-H. Detection of high-impedance fault in low-voltage DC distribution system via mathematical morphology. *J. Int. Counc. Electr. Eng.* **2016**, *6*, 194–201. [CrossRef]
14. Qi, P.; Jovanovic, S.; Lezama, J.; Schweitzer, P. Discrete wavelet transform optimal parameters estimation forarc fault detection in low-voltage residential power networks. *Electr. Power Syst. Res.* **2017**, *143*, 130–139. [CrossRef]
15. Santos, W.C.; Lopes, F.V.; Brito, N.S.D.; Souza, B.A. High impedance fault identification on distribution networks. *IEEE Trans. Power Deliv.* **2017**, *32*, 23–32. [CrossRef]
16. Li, M.; Jia, K.; Bi, T.; Yang, Q. Sixth harmonic-based fault location for VSC-DC distribution systems. *IET Eneration Transm. Distrib.* **2017**, *11*, 3485–3490. [CrossRef]
17. Chandra, A.; Singh, G.K.; Pant, V. Protection techniques for DC microgrid—A review. *Electr. Power Syst. Res.* **2020**, *187*, 106439. [CrossRef]
18. Namdari, F.; Salehi, M. High-speed protection scheme based on initial current traveling wave for transmission lines employing mathematical morphology. *IEEE Trans. Power Deliv.* **2017**, *32*, 246–253. [CrossRef]
19. Jia, K.; Li, M.; Bi, T.S.; Yang, Q.X. A voltage resonance-based single-ended online fault location algorithm for DC distribution networks. *Sci. China Technol. Sci.* **2016**, *59*, 721–729. [CrossRef]
20. Kavaskar, S.; Nalin, K. Combined mathematical morphology and data mining based high impedance fault detection. *Energy Procedia* **2017**, *117*, 417–423.
21. Paz, F.; Ordonez, M. High-Impedance Fault Detection Method for DC Microgrids. In Proceedings of the 2019 IEEE 10th International Symposium on Power Electronics for Distributed Generation Systems (PEDG), Xi'an, China, 3–6 June 2019; pp. 787–792.
22. Artale, G.; Cataliotti, A.; Cosentino, V.; Cara, D.D.; Nuccio, S.; Tiné, G. Arc fault detection method based on CZT low-frequency harmonic current analysis. *IEEE Trans. Instrum. Meas.* **2017**, *66*, 888–896. [CrossRef]
23. Qu, N.; Wang, J.; Liu, J. An arc fault detection method based on current amplitude spectrum and sparse representation. *IEEE Trans. Instrum. Meas.* **2019**, *68*, 3785–3792. [CrossRef]
24. Russell, B.D.; Chinchali, R.P.; Kim, C.J. Behaviour of low frequency spectra during arcing fault and switching events. *IEEE Trans. Power Del.* **1988**, *3*, 1485–1492. [CrossRef]
25. Fortuna, L.; Buscarino, A. Non-Intrusive Load Monitoring. *Sensors* **2022**, *22*, 6675. [CrossRef] [PubMed]
26. Fortuna, L.; Buscarino, A. Nonlinear Technologies in Advanced Power Systems: Analysis and Control. *Energies* **2022**, *15*, 5167. [CrossRef]